1-28-2014

Dynamical monodromy

C Chen

Megan K. Ivory
William & Mary

Seth Aubin
William & Mary, saaubi@wm.edu

J. B. Delos
William & Mary, jbdelos@wm.edu

Recommended Citation

Dynamical monodromy

C. Chen, M. Ivory, S. Aubin, and J. B. Delos[*]

Department of Physics, College of William and Mary, Williamsburg, Virginia 23187, USA

(Received 5 July 2013; published 28 January 2014)

Integrable Hamiltonian systems are said to display nontrivial monodromy if fundamental action-angle loops defined on phase-space tori change their topological structure when the system is carried around a circuit. In an earlier paper it was shown that this topological change can occur as a result of time evolution under certain rather abstract flows in phase space. In the present paper, we show that the same topological change can occur as a result of application of ordinary forces. We also show how this dynamical phenomenon could be observed experimentally in classical or in quantum systems.

I. INTRODUCTION

The general goal of this type of research is to understand and control quantum systems by understanding and controlling the corresponding classical systems. In recent years there have been major advances in classical mechanics: nonlinear dynamics, chaos theory, the "butterfly effect," new understanding of periodic orbits and their bifurcations and proliferation and their organization into families, chaotic transport and fractals, and some recently uncovered phenomena called "Hamiltonian monodromy." In each case, new understanding of classical systems has led to new understanding of their quantum counterparts.

This paper deals with the last-mentioned topic. We display new aspects of Hamiltonian monodromy in classical systems, and we show how these phenomena might be observed in a macroscopic system and in a system of ultracold atoms.

The proper name of our topic is "dynamical manifestations of nontrivial monodromy of action and angle variables in Hamiltonian systems." Let us just call it "dynamical monodromy." Monodromy means "once around a closed path"; a system exhibits "nontrivial monodromy" if when we go around a closed path in some space, the system does not come back to its original state. The simplest example of functions that have nontrivial monodromy are $f(z) = z^{1/2}$ or $g(z) = \log(z)$ for complex z: On one circuit around the branch point, $z = 0$, these functions change their values. A function of two real variables (l,h) with the same property is $\alpha(l,h) = l \tan^{-1}(h/l)$. If l represents angular momentum and h represents energy, and we multiply by constants to get the units consistent, then this function gives an approximate formula for an action variable of the system we will study: It is a multivalued function of (l,h), and on one circuit around the origin of (l,h) space, it changes its value.

A Hamiltonian system is said to exhibit nontrivial monodromy if the system is integrable and action and angle variables can be constructed, but they are found to be multivalued. Angle variables are defined in such a way that they trace out fundamental loops on tori. For the systems we are considering, the angle variables change smoothly as (l,h) change, but when (l,h) undergo a circuit around the origin, the loops change their topological structure. Specifically, a

loop that begins entirely on one side of a classically forbidden region ends by encircling that forbidden region. This is called a "static" manifestation of monodromy because it involves smooth connections among coordinates defined on "static" tori.

In Refs. [1,2] it was pointed out that this static manifestation of monodromy must have dynamical consequences: If a collection of particles is given initial conditions corresponding to an initial angle loop on a torus, and those particles are driven continuously around a monodromy circuit, then the loop of particles must undergo the same topological change that is seen in the angle loop.

The purpose of this paper is to answer two questions. (1) Can this phenomenon be seen using ordinary particles that obey Newton's laws of motion? (2) Can it be seen under less-than-ideal conditions, with particles having a distribution of energies and angular momenta? We show in this paper by computation that the answer to both of these questions is "Yes." We also present a design for an experimental measurement that would answer another question. (3) What happens in a quantum system? To what extent will these phenomena show up in an ultracold gas or a Bose-Einstein condensate?

In the next section we give a general introduction to Hamiltonian monodromy, so that we can pose questions (1) and (2) with more mathematical precision. Then in Sec. III we establish by computation affirmative answers to questions (1) and (2). Finally in Sec. IV and Appendix C we present designs for two experimental implementations of the theory. One is purely classical, involving pucks on a tilting air table, while the other, an ultracold gas or a BEC, brings forth quantum-mechanical issues that are not addressed by the computations presented in this paper.

II. STATIC AND DYNAMICAL MANIFESTATIONS OF MONODROMY

A. Tori and torus quantization

Let us begin with the primary theorem on bound integrable systems [3]. Given a phase space of dimension $2N$ with coordinates $\mathbf{z} = (z_1, \ldots, z_{2N}) = (q_1, \ldots, q_N, p_1, \ldots, p_N) = (\mathbf{q}, \mathbf{p})$, suppose there are N independent functions $\{F_\alpha(\mathbf{q}, \mathbf{p}) | \alpha = 1, 2, \ldots, N\}$ "in involution" with each other, i.e., their mutual

———————
[*]Corresponding author.

Poisson brackets all vanish,

$$[F_\alpha(\mathbf{z}), F_\beta(\mathbf{z})] = \sum_i (\partial F_\alpha/\partial q_i)(\partial F_\beta/\partial p_i)$$
$$- (\partial F_\alpha/\partial p_i)(\partial F_\beta/\partial q_i) = 0. \quad (1)$$

We use lowercase letters f_α to represent the values of these functions, and we call the space of values $\{f_\alpha | \alpha = 1, \dots, N\}$ of these functions "spectrum space."

We examine the level sets Λ_f of these functions—the set of phase-space points $\mathbf{z}$ such that all $F_\alpha(\mathbf{z})$ are constants, f_α:

$$\Lambda_f = \{\mathbf{z} | F_\alpha(\mathbf{z}) = f_\alpha, \alpha = 1, ..., N\}. \quad (2)$$

The "Liouville-Arnold" theorem asserts that any such level set that is compact and connected is topologically equivalent to a torus [3]. Furthermore there exists a set of action and angle variables which make good coordinates for the tori. Each angle variable $\phi_i(\mathbf{z})$ varies from 0 to 2π when the phase-space point $\mathbf{z}$ goes around one of the fundamental loops of a torus, while the action variables $I_i(\mathbf{z})$ are constant on each torus because they depend on $\mathbf{z}$ only through their dependence on the set of functions $\mathbf{F}(\mathbf{z})$: $I_k(\mathbf{z}) = \mathscr{I}_k(F_1(\mathbf{z}), \dots, F_N(\mathbf{z}))$. It is presumed that the Hamiltonian function for the physical system depends only on the functions $F_\alpha(\mathbf{z})$; there is presumed to be an invertible relationship between values $\mathbf{f}$ of these conserved quantities and values $\mathbf{i}$ of the action functions, so the Hamiltonian can also be expressed as a function of the action variables, $H(\mathbf{z}) = \mathscr{H}[I(\mathbf{z})]$. It follows that the motion of any phase-space function $g(\mathbf{z})$ is quasiperiodic (i.e., a Fourier transform of $g[\mathbf{z}(t)]$ shows N fundamental frequencies and all harmonics and combinations), and the fundamental frequencies ω_i are simply obtained from the Hamiltonian by differentiation, $\omega_j = \partial \mathscr{H}(I)/\partial I_j$. Also, good approximations to quantum eigenvalues and eigenfunctions are obtained by examining a discrete set of tori having appropriately quantized values of action variables.

These concepts, first formulated by Liouville, carried into the old quantum theory by Einstein in 1918, and revived starting in the 1970s by Percival [4–6], Marcus and Noid [7–16], and Berry [17], are a standard part of the repertoire of semiclassical physics and chemistry [18]. They have been used to study an immense variety of systems, such as simple nonlinear oscillators (e.g., the Henon-Heiles system) [19–22], molecular vibrations and rotations [23], excited states of hydrogen in electric and magnetic fields [24,25], doubly excited states of helium [26–28], spin-orbit coupling [29], and excited states of nuclei [30]. (Googling the phrase "torus quantization" gives over 3000 hits.) Torus quantization also arises in problems far afield from atomic, molecular, and optical (AMO) physics: In a study of a Buffon probability problem (when a needle is dropped in random positions on a tiled floor, what is the probability that the needle intersects n of the lines between the tiles?), it was found that torus quantization gives a step on the path to the solution [31]. Analysis and quantization of tori have been widely studied for so many years that it might come as a surprise that reexamination of the theory would lead to new and interesting phenomena.

B. Singular points and monodromy

In this beautiful and well-known theory, it is easy to fail to notice the little assumption that the functions $F_\alpha(\mathbf{z})$ must be independent, i.e., their phase-space gradient vectors $\nabla_\mathbf{z} F_\alpha(\mathbf{z})$ must be linearly independent. However, in many systems there are points $\mathbf{z}_s$ at which the functions fail to be independent (among other things, one or more of the gradients might vanish). Phase-space points $\mathbf{z}_s$ at which the rank of the $N \times 2N$ matrix $DF = \partial F_i/\partial z_j$ is less than N are called singular points, and the corresponding values of the conserved quantities $\mathbf{F}(\mathbf{z}_s) = \mathbf{f}_s$ are called singular values. A value $\mathbf{f} = \mathbf{F}(\mathbf{z})$ is "regular" only if no phase-space point $\mathbf{z}$ in its preimage under $\mathbf{F}$ is singular, otherwise it is a singular value. A region of spectrum space is called "regular" if and only if all values of $\mathbf{f}$ in that domain are regular.

The importance of singular values is that *near such singular values*, *the structure of the embedding of tori in phase space might change*. A trivial example is a one-dimensional pendulum, in which $H = p^2/2 - \cos q$. Phase-space points $\mathbf{z}_- = (\mathbf{q} = 0, \mathbf{p} = 0)$ and $\mathbf{z}_+ = (\mathbf{q} = \pi, \mathbf{p} = 0)$ are singular (the gradient of H vanishes there), and the singular values are $E_- = H(\mathbf{z}_-) = -1, E_+ = H(\mathbf{z}_+) = 1$. For $E < -1$ there are no tori, while for each energy in the interval $-1 < E < 1$, a single torus corresponding to librational motion exists. For $E > 1$, we find at each value of E two tori, corresponding to rotation in a clockwise or counterclockwise sense. Thus at each of the singular points $E = \pm 1$, there is a structural change.

More substantial examples are given in the book by Cushman and Bates [32]. This book examines simple mechanical systems that appear in undergraduate textbooks (two-dimensional harmonic oscillators, tops, spherical pendula, etc.) and uses modern mathematical artillery to study them—Poisson algebras, Lie theory, Ehresmann connections, Morse theory, bifurcation theory, and especially global analysis. Global analysis focuses on how tori foliate phase space smoothly, or how the embedding of tori in phase space can change abruptly near a singular value.

Duistermaat [33] (apparently following a suggestion of Cushman) was the first to publish a paper discussing nontrivial consequences of singular values. Consider a system with two degrees of freedom having a Hamiltonian of the familiar kinetic plus potential energy form, in which the potential energy is cylindrically symmetric:

$$H(\boldsymbol{p}, \boldsymbol{q}) = \frac{\boldsymbol{p}^2}{2} + V(\rho) = h, \quad (3)$$

$$\rho = \sqrt{x^2 + y^2}, \quad (4)$$

$$V(\rho) = -a\rho^2 + b\rho^4 \quad (a, b > 0). \quad (5)$$

The potential-energy function has a well to confine particles within a certain region and a central potential-energy barrier. Conserved quantities are the angular momentum $L = xp_y - yp_x$, with numerical value $L(\mathbf{p}, \mathbf{q}) = l$ and the Hamiltonian $H(\mathbf{p}, \mathbf{q}) = h$. The derivatives of both $H(\mathbf{p}, \mathbf{q})$ and $L(\mathbf{p}, \mathbf{q})$ vanish at the origin in phase space $(x, y, p_x, p_y) = \mathbf{0}$, and therefore it is a singular point, and the corresponding origin in

spectrum space $(l,h) = \mathbf{0}$ is a singular value, or monodromy point.

A closed directed path $[l(s),h(s)]$ in spectrum space surrounding this singular value is called a monodromy circuit (s is a continuous timelike variable representing points along the path). If the canonical action functions $\mathscr{I}_k(l,h)$ are defined so that they vary smoothly as the system is carried around this circuit, then, when the system returns to the original (l,h), one of the action functions is changed. One of the two action functions is always

$$\mathscr{I}_1(l,h) = \frac{1}{2\pi} \oint L(\mathbf{z})d\phi = l,$$
$$I_1(\mathbf{z}) = L(\mathbf{z}) = xp_y - yp_x,$$

(6)

so it does not change when we carry the system around the monodromy circuit,

$$\mathscr{I}_1^f(l,h) = \mathscr{I}_1^i(l,h) = l^i = l^f$$

(7)

(superscripts i and f mean initial and final). The other action variable can initially be taken to be an integral around a "ρ loop":

$$\mathscr{I}_2^i(l^i,h^i) = \frac{1}{2\pi} \oint p_\rho(\rho;l,h)d\rho.$$

(8)

However, at the end of the monodromy circuit, this action function has changed to [33–35]

$$\mathscr{I}_2^f(l^f,h^f) = \mathscr{I}_2^i(l^i,h^i) - \mathscr{I}_1(l^f).$$

(9)

$\mathscr{I}_2$ is therefore a multivalued function of (l,h). The conjugate angle variables must also change on a passage around the monodromy circuit:

$$\phi_1^f = \phi_1^i + \phi_2,$$

(10)

$$\phi_2^f = \phi_2^i = \phi_2.$$

(11)

It is easy to verify that the transformation from $(\phi_1^i,\phi_2^i,I_1^i,I_2^i)$ to $(\phi_1^f,\phi_2^f,I_1^f,I_2^f)$ is canonical.

In Fig. 1, we show this static manifestation of monodromy. The figure in the center is a monodromy circuit in (l,h) space; in this case, any counterclockwise circuit surrounding the origin gives the same result. The outer figures show seven tori corresponding to seven different points in the (l,h) spectrum space. The tori are represented in (x,y,p_ρ) space [it is convenient to regard (x,y,p_ρ) as orthogonal axes]. When the system is carried around such a circuit surrounding the origin in (l,h) space and it returns to the original torus, the coordinate system defined by canonical angle variables on the tori changes smoothly into a different one. (The method used to calculate angle loops is given in Appendix A.)

On each torus two families of fundamental loops $[\gamma_1]$ (green curves online) and $[\gamma_2]$ (blue curves online) are shown, and they provide a coordinate system for each torus. Each toroidal loop γ_1 (green online) has a constant value of canonical angle variable ϕ_2, while ϕ_1 varies from zero to 2π. These loops are spaced by fixed steps of ϕ_2. Likewise each poloidal loop γ_2 (blue online) has a constant ϕ_1, while ϕ_2 varies from zero to

2π. Those loops are spaced by fixed steps of ϕ_1. One of the γ_2 loops is stressed by a heavy curve (black online).

The fundamental loops and the associated coordinate systems in the tori change smoothly as l and h change. Starting at $l = 0$, $h = -35$, the stressed γ_2 (heavy black loop) is perpendicular to the toroidal (green online) loops, and it is projected into the (x,y) plane as a line. Moving counterclockwise in the (l,h) plane, that loop is widened and tilted. For $h > 0$, as l decreases from $(l,h) = (5,6)$ to $(0,5)$, the "doughnut hole" shrinks, and the innermost point of any poloidal γ_2 loop approaches the origin in (x,y,p_ρ) space. For $l = 0$ this (x,y,p_ρ) projection of the torus is singular, and the γ_2 loops all rise vertically through the origin. When l continues to decrease for $h > 0$, the formerly poloidal (blue online) loops all go around the doughnut hole, and their projections into the (x,y) plane enclose the origin. Continuing around the monodromy circuit, the loops change smoothly; when we get back to the original torus $l = 0$, $h = -35$ the loops γ_2, and the associated canonical angle coordinate system, are topologically different from the original loops on that torus. The originally poloidal loop now goes around the torus in both poloidal and toroidal senses.

Also, examining the projections of the γ_2 loops into the (x,y) plane, wherein there is a classically forbidden region surrounding the origin, the topology of the projected loop has changed. Initially it is a "trivial" loop, which in configuration space could be shrunk to a point without passing through the forbidden region, while at the end it has winding number -1 about the forbidden region.

At the top of the monodromy circuit, at $(l = 0, h = 5)$ the (x,y,p_ρ) representation of the torus is singular. However, the torus itself and its basic loops are not singular there. To display this, we show in the top line of Fig. 1 a representation of the tori in another space, $(X = y + p_x,\ Y = y - p_x,\ P_y = x + p_y)$, where the tori and the poloidal loops (blue and black online) evolve smoothly from $(l = 5,\ h = 6)$ to $(l = -5,\ h = 4)$. This change of the topological structure of the family of fundamental loops $[\gamma_2]$ is a static manifestation of monodromy.

Quantum implications of multivalued action variables were first described by Cushman and Duistermaat [36]: The lattice of allowed semiclassical eigenvalues $\{E_{n,m}\}$, defined such that $\mathscr{I}_2(m,E_{n,m}) = (n + 1/2)\hbar$, $\mathscr{I}_1(m) = m\hbar$ has a defect. The global perspective was brought into AMO physics especially by Sadovskii, Zhilinskii, and their colleagues. They have used the new methods to show the presence of monodromy and related phenomena in the hydrogen atom in perpendicular fields [37–39], the CO_2 molecule [40–42], HCN [43], LiCN [44], systems with coupled angular momenta [45,46], and a number of model oscillator systems [47–49]. Quasilinear molecules are discussed at length in [50–52], diatomic molecules in fields in [53], and the hydrogen atom in tilted fields in [54,55]. Experimental observations in a classical swing-spring system were made in [56].

C. A dynamical manifestation of monodromy

The above discussion describes the properties of angle coordinates on each (l,h) torus, and how those coordinate systems change if we compare one torus with another. We call
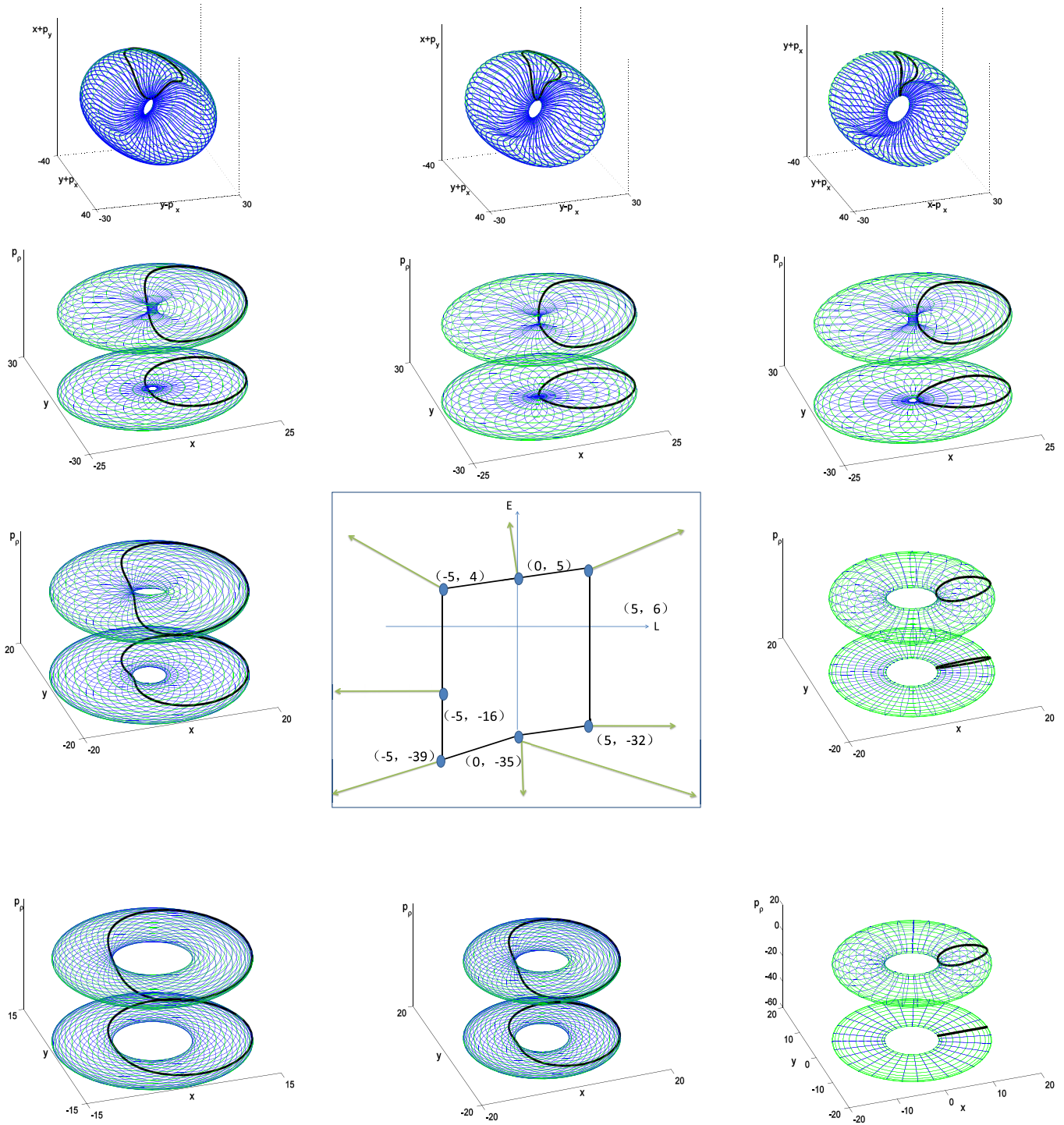
FIG. 1. (Color online) A static manifestation of Hamiltonian monodromy. Explanation is given in Sec. II B.

the phenomenon illustrated in Fig. 1 a static manifestation of monodromy because it is a property of static coordinate systems on static tori. A time variable t never appears in Sec. II B above; there is a path variable s for the monodromy circuit $(l(s),h(s))$, but motion in real time is not considered. Therefore it may seem that monodromy is an abstract geometrical property of abstract variables, with no interesting dynamical consequences. However, we now know that monodromy has significant dynamical consequences [1,2].

What happens if in addition to the forces represented by the Hamiltonian $H(\mathbf{z})$, we subject the system to an *additional* perturbing flow in phase space that changes the angular momentum and energy of particles in the system? Such additional forces and torques drive particles from one torus to another.

Specifically, suppose we begin with a collection of noninteracting particles on an initial torus having ($l = 0$, $h < 0$), and suppose that the positions and momenta of these particles

correspond to the initial γ_2 loop. Suppose then that all particles are made to change their angular momentum and their energy simultaneously, so that at every instant all particles have equal angular momentum and energy. Suppose furthermore that as they are driven from one torus to another, the change of torus leaves the value of the angle variables unchanged. (This statement requires a definition of the origin of coordinates on each torus, which we give in Appendix A.) Then the angle variables evolve with time as

$$\frac{d\boldsymbol{\phi}}{dt} = \boldsymbol{\omega}(l(t),h(t)). \tag{12}$$

We may think of this evolution as occurring in incremental steps. In the first half of each step, the particles move along a static torus with $d\phi/dt = \boldsymbol{\omega}(l,h)$, and in the second half of each step, each particle moves from a point on one torus to a point on an adjacent torus in such a way that the numerical values of the angle variables are unchanged $\boldsymbol{\phi}(l,h) = \boldsymbol{\phi}(l + dl, h + dh)$. We call this process "ideal" evolution. It is ideal in two senses: (i) the particles all begin on a single loop on a single torus, and that loop has a constant value of the angle variable ϕ_1^i; (ii) the particles move synchronously from one loop to another. This process is one type of ideal evolution.

Now suppose that the perturbing flow carries the particles in this way around a monodromy circuit in real time. In [2] we gave a full description of such "ideal" evolution, and we showed that a collection of particles distributed around a γ_2 loop remains always distributed around a γ_2 loop. At the end of the monodromy circuit, when all particles have returned to the original torus, they occupy the final γ_2 loop; that is, they have gone from a loop that is on one side of the potential-energy barrier to a loop that surrounds the potential-energy barrier. Thus the change in the angle coordinates on the tori is manifested in the dynamical behavior in real time.

The work in those references [1,2] left two important questions unanswered. (1) The ideal evolution defined therein arises from application of a perturbing flow in phase space which is (or can be) a Hamiltonian flow, but which cannot be derived from a single-valued Hamiltonian function. Can we implement a monodromy circuit by application of ordinary forces? (2) In any real system, the initial conditions cannot be a perfect γ_2 (poloidal) loop defined on a single torus; particles will have a distribution of initial angles, initial angular momenta, and energies. Can a monodromy circuit be implemented in a real system?

III. SIMULATIONS AND RESULTS

In this section, we show by computation that the answers to the two questions given at the end of Sec. II are "yes": (1) a monodromy circuit can be achieved by the application of ordinary forces, and (2) it can be achieved under reasonable experimental conditions. We have carried out calculations on a variety of two-dimensional circularly symmetric potential energies having a well and a central barrier, comparable to that given in Eq. (5). To change the angular momenta of the particles, we apply a torque. Also, since raising and lowering the energy of the particles would not be easy to implement in an experiment, we instead lower and raise the central barrier

(or equivalently, raise and lower the potential well). To answer the two questions separately, we carry out the calculations under two sets of initial conditions.

Single loop initial conditions (case a). We suppose that initially the particles all have the same energy and angular momentum, so their phase points lie on a single torus; we suppose that the particles are uniformly distributed on a single initial γ_2 loop on that torus, similar to the stressed (black online) loop in Fig. 1. Note that whereas the particles initially all have the same angular momentum and energy, as soon as a transverse force is applied, with the same force on all particles, each particle experiences a different torque, so their angular momenta do not remain equal. Also as the potential energy changes, they gain and lose different amounts of energy. However, the particles always occupy a single loop in phase space. That loop is close to a corresponding loop on a single torus, provided that the perturbing forces are applied slowly and gently, so that they do not change much during a radial oscillation of the particles. This is a kind of adiabatic implementation of the monodromy circuit. In our calculations, the entire monodromy circuit is implemented in approximately 30 cycles of radial oscillation. (Further discussion of adiabaticity is in Appendix D).

Cold-gas initial conditions (case b). The Heisenberg uncertainty principle tells us that we cannot fix both the angle and the angular momentum of particles, and practical experimental limitations tell us that we cannot fix the energy exactly. We suppose that the initial conditions involve a range of initial angles and angular momenta and energies, so that the phase-space points of the particles lie on different tori, but all are reasonably close to the initial γ_2 loop of case (a). The spread of angular momenta, angles, and energies is consistent with what can be done experimentally for a cold gas described in Sec. IV, so we call this case "cold-gas initial conditions." Again the applied forces change slowly compared to the period of radial oscillation. (However, note that if the forces change too slowly, so that the time required to go around the monodromy circuit is too long, then the gas particles will spread because of their thermal motion, and the change of character of the loop will not be visible. Computational experience has shown that the topological change is visible when the entire monodromy circuit is implemented in about 30 cycles of radial oscillation.)

To drive the particles around the monodromy circuit we use the following five steps. Every step is done sufficiently slowly that there are several radial oscillations of the particles in each step. In computations, we can start a collection of particles distributed around a single loop with zero angular momentum and fixed energy, or distributed with a broader range of initial angular momenta and energy comparable to the single-loop initial conditions. However, in an actual experiment, it is easier to start particles in a small packet near the inner turning point. Then after they have moved to the desired position, the process described below is begun.

(1) Keeping the cylindrically symmetric potential unchanged, add a rotating force $\boldsymbol{F}(t)$, the same force on all particles, to increase their angular momenta. The force is turned on and off gently and, in case (a), its direction is kept perpendicular to the position vector of the center of mass of the loop of particles. As a result, the force rotates counterclockwise

with a frequency close to

$$f = \frac{\Delta(\bar{l},\bar{h})}{\tau(\bar{l},\bar{h})}. \tag{13}$$

$\tau(l,h)$ and $\Delta(l,h)$ are, respectively, the "radial period" or time of first return, and the angle subtended in that time on the torus having angular momentum and energy respectively equal to (l,h). $\bar{l}$ and $\bar{h}$ are the mean values of angular momentum and energy at the time t (see Appendix A).

(2) Turn off the rotating force and raise the potential well so as to increase the energies of the particles to positive values. Equivalently, we may lower the central barrier; particle energies are defined relative to the value of the potential energy at the origin $\rho = 0$.

(3) Keeping the cylindrically symmetric potential fixed at the new values, apply the rotating force again the opposite way to reduce the angular momenta until they are negative. Again that force must rotate counterclockwise at a frequency close to that given in Eq. (13). In the "single-loop" computations of case (a) we keep the force perpendicular to the vector from the origin to the center of mass of the family of particles.

(4) Turn off the rotating force and lower the well to its original depth; this decreases the energy of each particle. Equivalently, we may raise the central barrier to its original height.

(5) Keeping the potential-energy function fixed at the new values (equal to the original values), apply the rotating force, still rotating counterclockwise with frequency (13), to increase the angular momentum of the particles, until the average angular momentum of those particles equals zero. Calculation shows that the average energy is then close to the initial energy.

Additional details about the potential energy and the perturbations are given in Sec. IV and Appendix B.

Figure 2 shows the resulting monodromy circuit for "single-loop initial conditions" and for "cold-gas initial conditions."
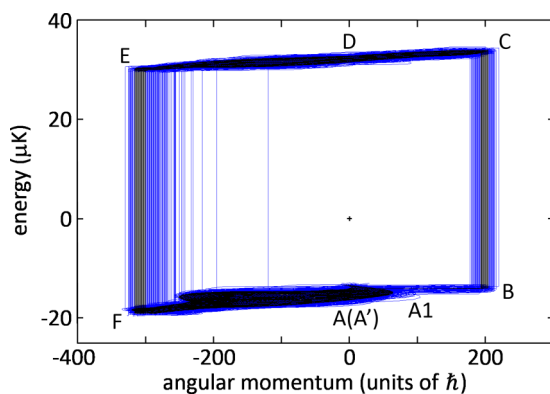

FIG. 2. (Color online) Spectrum-space paths, i.e., paths in angular momentum—energy space, (l,h). Each line represents the path $[l(t),h(t)]$ of one particle as it travels around the monodromy circuit starting at point A and proceeding through A1, B–F, and back to the final point A (called A′). Black lines represent particles with initial conditions on a single loop, and gray lines (blue online) are paths of particles having cold-gas initial conditions. Particles are driven around the monodromy circuit by applying a common force acting as a torque to change the angular momentum, and by raising or lowering the potential-energy well.

We see that the particles gain different amounts of energy and angular momentum as they traverse the monodromy circuit. However, they stay adequately close in angular momentum and energy.

Figure 3 shows the configuration space and velocity space behavior for the single loop and for cold-gas initial conditions. Two important things are shown by this simulation. First, it is possible to drive a collection of particles around a monodromy circuit using ordinary forces (rather than by using the ideal flow defined in Ref. [2]). Second, while we already know that the changed structure of the loop in configuration space provides a definitive signature of monodromy, also the structure in velocity space provides another clear signature.

Thus we have shown by computation that this dynamical manifestation of monodromy can be implemented in a real system by application of ordinary forces.

IV. EXPERIMENTAL REALIZATION

In this section and in Appendix C, we outline two experimental schemes for observing dynamical monodromy. The scheme described in the appendix uses motion of a magnetic puck on an air table, so it is a purely classical realization of the theory. The scheme described below uses a gas of ultracold atoms to implement dynamical monodromy. This experiment also offers the possibility of exploring the phenomenon in the presence of interparticle interactions, as well as quantum-mechanical effects such as interference and tunneling, which are beyond the scope of the theory presented in this paper. It is not an easy experiment, but it uses only standard tools of atomic physics.

A conclusive observation of dynamical monodromy should show experimentally that if one starts with a loop of initial condition points in phase space and then varies their energy and angular momentum along a closed path in spectrum space (such as in Fig. 2), then the initial and final configuration-space loops have a topologically different structure relative to the forbidden region surrounding the origin—i.e., the final, but not the initial loop encloses the energetically inaccessible region. The experimental system requires two main ingredients: (1) *precision control* for producing the initial phase-space loop, and for applying the torque and central potential barrier modulations to accurately implement the prescribed spectrum space path; and (2) *accurate measurements* of energy, angular momentum, position, and velocity to verify the phase-space and spectrum-space coordinates of the system at the start, end, and during the monodromy process.

The ultracold atoms scheme uses a ring-shaped optical trapping potential for ultracold ^{39}K atoms. Instead of running the full loop of initial conditions simultaneously, the atoms are placed in a short segment of the loop of initial conditions and then driven around the ring potential by the application of a uniform magnetic force, while the height of the central barrier is appropriately modulated to follow the monodromy circuit. The resulting energy and angular momentum of the atoms can then be tracked by both *in situ* and time-of-flight imaging as the system moves along the prescribed spectrum space path. The monodromy process for the full loop of initial conditions is reconstructed by combining the results of separate initial
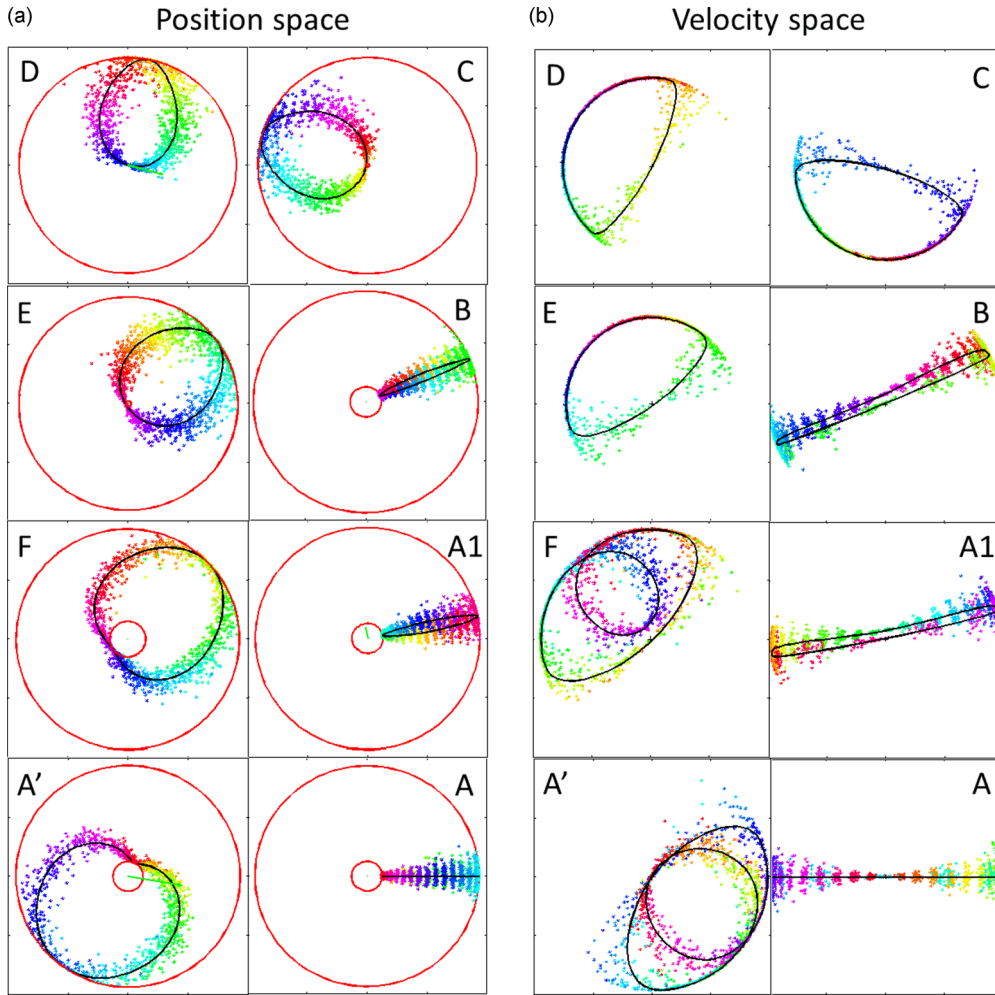
FIG. 3. (Color online) This is a collection of snapshots showing the evolution of the single loop and of the cold gas as the system traverses the monodromy circuit. The topological structure of loops of particles in configuration space changes during the monodromy circuit. Single-loop initial conditions are represented by the solid (black online) curve, while gas particles are represented by dots (color online). (A) and (A′) are points marked in Fig. 2. (a) Position space. Each square is a region 400×400 μm ($\pm 200\,\mu$m about the origin). The inner and outer circles are boundaries of the classically allowed region for any single-loop particle that has $l = \langle l \rangle$ and $h = \langle h \rangle$. The vectors from the origin (green online) represent the applied rotating force. (A) Initially all single-loop particles have the same energy and angular momentum ($l = 0, h = h_0$) and they form a line in configuration space (x-y plane) while the "gas particles" have a spread in angle, angular momentum, and energy: $\langle h \rangle = h_0$, $\Delta h > 0$, $\langle l \rangle = 0$, and $\Delta l \Delta \phi = \hbar/2$. (A1) In the second snapshot, as angular momenta increase, the line evolves into a loop always linking the inner and outer boundaries. (B and C) The well is lifted (equivalently, the central barrier is lowered), so the central forbidden region is reduced to a size governed by the angular momentum. (C,D,E) With energy of the particles above the central barrier, the angular momentum is decreased from positive to negative. At some instant a single-loop particle having zero angular momentum passes over the center point $x = y = 0$; for that particle the central forbidden region has vanished for an instant. When it reappears, it is inside the loop. (E and F) The well is lowered (equivalently, the barrier is raised) and the central forbidden region gets larger. (F and A′) The angular momentum is driven back up to zero. Integration is stopped when $\langle l \rangle = 0$, and we find that $\langle h \rangle$ is close to the initial energy, h_0. Like the angle loop γ_2, the loop of particles has evolved into a topologically different loop. (b) Momentum space, (p_x, p_y). The units of momentum are 10^{-27} Kg m/s. Each square is a region 20×20, extending from ± 10 about $\mathbf{p} = \mathbf{0}$. From points A1–C, the loop does not enclose the origin. At D it touches the origin, and from E–A′, the winding number about the origin is 1. Initially particles are traveling equally to the left and right. At the end, they are dominantly going in a beam like a rotating searchlight.

condition segments, so that the new topology of the resulting phase-space distribution can be observed.

The experimental implementation requires a number of lasers to produce a ring potential and several external magnetic fields to produce a torque that changes the angular momentum of the atoms. Figure 4 shows how lasers and magnetic coils can be combined to produce the appropriate optical potential and magnetic force for the atoms, which are then detected

by a high resolution imaging system. We summarize the main suggested experimental parameters in Table I. In the following paragraphs, we describe the details of the ring trap, the atomic packet and its preparation in a segment of the ring of initial conditions, the torque force, and how to measure the total energy and angular momentum of the atomic packet.

Ring trap. The atoms are confined in a ring trap produced by two blue-detuned optical dipole potentials produced by two
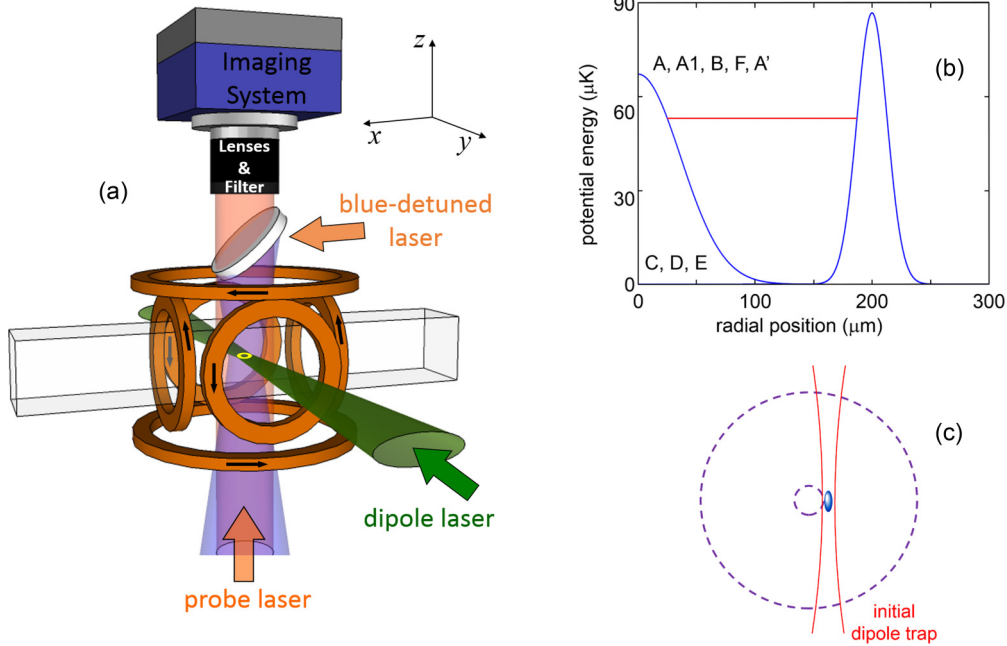
FIG. 4. (Color online) Proposed apparatus and optical potentials for observing dynamical monodromy. (a) Sketch of apparatus for observing dynamical monodromy: The atoms are confined in a ring trap formed by the vertical downward-directed blue-detuned laser beams and the horizontal laser beam (green online). The ring trap is the light (yellow online) ring in the intersection of these beams. Coils (orange online) generate magnetic fields for tuning the interactions to zero and producing the torque force. The camera is used for absorption imaging with an upward-directed laser probe beam (up-pointing arrow, orange online). (b) Planar ring-trap potential for the ultracold ^{39}K atoms. The potential consists of a central Gaussian barrier with a waist radius of 73 μm and an outer Gaussian wall at a radius of 200 μm with a waist of 26 μm. (c) Trap and release method for producing the atomic packet with total energy 53 μK.

vertically directed laser beams: a focused laser that serves as the central barrier and a concentric hollow laser beam that provides the outer wall of the trap. Hollow beams can be generated with a variety of optical elements such as axicon lenses [57], phase plates [58], and spatial light modulators [59]. Time-averaged doughnut beams can be produced by rapid rotation of a Gaussian beam using two crossed acousto-optic modulators [60]. The Gaussian ring potential of Fig. 4(b) is well suited for ultracold atom monodromy studies and can be produced with central barrier and outer wall laser powers of 0.4 and 2.5 W, respectively, at 750 nm. An additional red-detuned laser can be used to form a horizontal sheet of light that provides vertical confinement, while leaving the horizontal confinement potentials negligibly affected: For example, a 10 W laser beam at 1064 nm focused to horizontal and vertical

TABLE I. Summary of ultracold atom experiment parameters.

Parameter	Value
Ring-trap laser power	2.9 W at 750 nm
Vertical trapping laser power	10 W at 1064 nm
Atomic state	$\lvert F = 1, m_F = +1 \rangle$ hyperfine state of ^{39}K
Atomic packet population	4×10^4
Energy of initial atomic packet	53 μK
Peak torque force	0.36 m$_K$g*
Magnetic Feshbach zero	350 G
Duration of monodromy round trip	100 ms

*I.e. 0.36 times the weight of a potassium atom.

waist radii of 5 mm and 30 μm, respectively, will provide harmonic confinement of 360 Hz along the vertical axis with a trap depth of roughly 4 μK, but with a negligible 2 Hz confinement in the horizontal plane. Alternatively, vertical confinement can be provided by a one-dimensional optical lattice of horizontal "pancake traps" with the atoms spread over multiple layers. Based on simulations of atomic motion in the ring potential, the average scattering rate from all of the far off-resonant trapping light is estimated to be about 1 Hz per atom and so is negligible over the 100 ms duration of the proposed experiment.

Atomic packets. The atomic packets consist initially of a noninteracting Bose-Einstein condensate (BEC) of ^{39}K atoms designed to minimize the expansion of the atomic packet as it follows the spectrum space path. The BEC limits the expansion of the atomic packet to the Heisenberg-limited spread required of all quantum-mechanical systems, but must be carefully tailored by choosing an appropriate initial packet size: In our case, a ^{39}K BEC with radial and tangential half-widths of 0.3 and 2.25 μm, respectively, will expand with respective velocities of 2.7 and 0.4 μm/ms. Repulsive atom-atom interactions can also lead to relatively large expansion rates, but can be sufficiently suppressed by using the $\lvert F = 1, m_F = +1 \rangle$ hyperfine ground state of ^{39}K at a magnetic field of 350 G, which tunes the s-wave scattering length to zero due to a nearby Feshbach resonance [61]. (A slightly attractive interaction may be useful in reducing the Heisenberg-limited spreading of the packet, though simulating its precise effects on the atomic packet is beyond the scope of this paper.) Experimentally, the interactions are difficult to
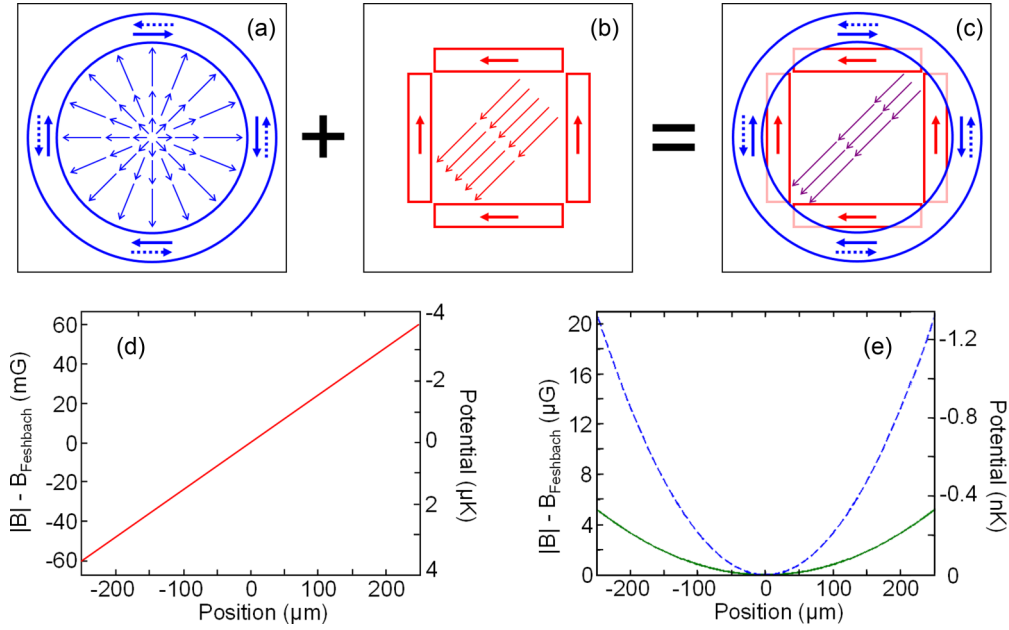
FIG. 5. (Color online) Magnetic fields for producing the torque force. The top three panels sketch how the quadrupole magnetic field [panel (a), thin arrows, blue online] generated by the anti-Helmholtz coil pair combines with the uniform horizontal magnetic field [panel (b), thin arrows, red online] produced by the two Helmholtz coil pairs to produce a magnetic gradient in the direction of the magnetic field [panel (c), thin arrows, purple online], whose orientation is determined by the relative currents in the two Helmholtz coil pairs. The magnetic field line sketches in panels (a), (b), and (c) are all in the horizontal plane (view from above) and are not to scale: The thick arrows represent the current in the coil, while the thick dashed arrows indicate the current in the hidden coil underneath. The two plots (d) and (e) show the magnetic field magnitude and its associated effective potential. Along the field direction (d) it is nearly linear (red online) while in the transverse directions (e) it is quadratic: Its horizontal variation is represented by the solid (green online) curve, and its vertical variation by the dashed (blue online) curve. Note the reversed right axes for the potential energy, since the $|F = 1, m_F = +1\rangle$ state is a strong field seeker.

eliminate altogether, but even if the scattering length is reduced to $a_s = 0.17a_0$, which for $\partial a_s / \partial B = 0.55a_0$ [61] corresponds to a magnetic field tuning precision of $\Delta B = \pm 0.3$ G, then interaction-induced spreading is negligible for packets with fewer than 8×10^4 atoms. However, the atom number must also be sufficiently large to allow for high-quality imaging: Simulations of time-of-flight experiments, such as in Fig. 7, show that atom numbers of 4×10^4 or more produce final atomic packets with optical depths of 0.5 or higher, which are suitable for absorption imaging methods [62].

Initial conditions. The BEC is inserted into the ring trap with a multistep process. As shown in Fig. 4(c), the BEC is initially trapped by a single-beam optical dipole trap produced by an additional laser that copropagates with the 1064 nm laser sheet [not shown in Fig. 4(a)]. The BEC is located at a radius of 25 μm, which corresponds to a potential energy of 53 μK. Upon turning off this single beam confining potential, the BEC is free to oscillate in the ring potential. The specific position-velocity combination of the ring of initial conditions for the atomic packet is chosen by applying the torque force at the appropriate time of the oscillation phase. Our simulations show that a radial positioning error of ± 1.25 μm can be tolerated. Alternatively, if a higher precision method is needed, a multiphoton Bragg pulse [63,64] can be used to impart a momentum kick (corresponding to a kinetic energy of 53 μK) to BEC atoms held at the minimum of the ring potential.

Torque force. The torque force can be produced by the magnetic gradient of a horizontally oriented quadrupole coil

pair with equal and opposite currents in its two coils, as shown in Fig. 4(a). As illustrated in the top three panels of Fig. 5, the central symmetry quadrupole field combines with the 350 G horizontal magnetic field required for suppressing interactions. At 350 G, the Zeeman shift of the $|F = 1, m_F = +1\rangle$ hyperfine ground state is -1.33 MHz/G. Modulation of the torque force as shown in Figs. 6(a) and 6(b) help to reduce the width of the packet in spectrum space. A maximum force of 2.3×10^{-25} N $= 0.36$ mg is required, which corresponds to a magnetic gradient of 2.6 G/cm. The combination of the uniform 350 G field with the weak quadrupole field results in a magnetic gradient along the direction of the 350 G field, while the gradients in the transverse horizontal and vertical directions contribute negligibly to the potential over the size of the ring trap. The orientation of the magnetic torque force can be easily rotated in the horizontal plane by changing the direction of the 350 G field, which is generated by two orthogonal Helmholtz-style coil pairs: Sinusoidal modulation of the coil pair currents ($\pi/2$ out of phase from each other) rotates the 350 G field and the magnetic gradient in a manner similar to the magnetic field modulations in a time-orbiting potential (TOP) trap [65]. Figure 6(b) shows the orientation of the torque force and 350 G field over the course of the monodromy process: The field maintains an average angle of roughly $\pi/2$ with respect to the angular position of the atomic ensemble and is rotated at rates of up to 330 Hz, which is substantially slower than in a TOP trap [65]. Finally, the magnetic gradient produces a negligible variation of the
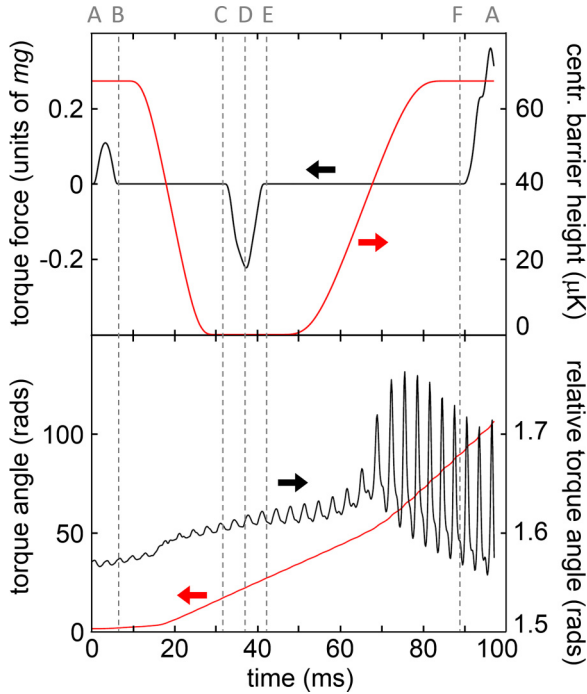
FIG. 6. (Color online) Torque force and central barrier modulation versus time required for completing the monodromy circuit. Top: Torque force magnitude (curve with arrow toward left axis, black online) and central barrier amplitude (curve with arrow toward right axis, red online) as a function of time. Bottom: Absolute torque angle with respect to starting position (arrow toward left axis, red online) and torque angle relative to full atomic ensemble center of mass (arrow toward right axis, black online). The letters on the top axis denote the monodromy circuit transit points of Fig. 2.

scattering length of at most $\Delta a_s = 0.06a_0$ over the roughly 400 μm diameter of the ring trap.

Measuring the total energy E. The total energy E of the atomic packet can be measured by turning off the outer laser barrier of the ring trap while the atoms are climbing the inner central barrier. The atoms convert all of their potential energy to kinetic energy as they are pushed away from the central barrier and leave the ring potential region, so that their average velocity, kinetic energy, and thus total energy can be measured by time-of-flight imaging.

Figure 7 shows the results of a simulation of this process. The method relies on the compactness of the atomic packet to guarantee that there are no atoms in the outer barrier region when it is turned off, and to ensure that a measurement of average velocity is representative for all the atoms in the packet. Numerical simulations show that the method functions well for all initial conditions and points along the spectrum space path: To measure the total energy E at some point along the spectrum space path, the monodromy process is stopped at the desired point, and the outer barrier is turned off as the atoms are climbing the central barrier. Furthermore, the instantaneous kinetic energy of the atoms can be measured by turning off the entire ring potential and then measuring the velocity by time-of-flight imaging. In practice, the 1064 nm optical dipole laser and the torque force magnetic gradient will need to be turned off as well, since they provide very weak but
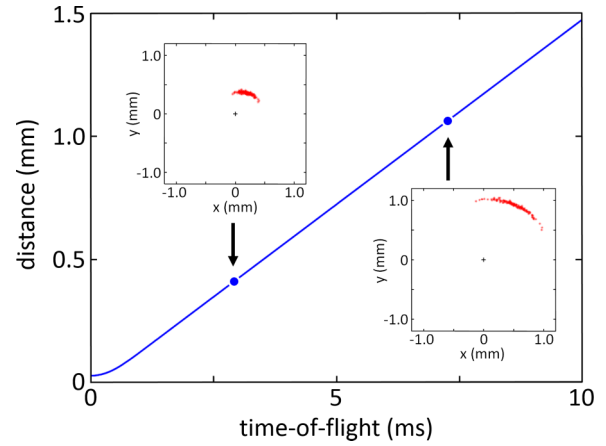

FIG. 7. (Color online) Time-of-flight method for measuring the total energy E. The plot corresponds to a packet that has completed the monodromy process and returned to point A (i.e., A′) on the spectrum space path of Fig. 2.

sufficient horizontal confinement to affect the time-of-flight measurements.

Measuring the angular momentum L. The angular momentum of the atomic packet can be measured by *in situ* imaging of the atoms as they travel around the ring potential. The inset of Fig. 8 shows a simulated image of the atoms in the ring potential, and the radially averaged atomic population as a function of angle from which the angular center of gravity of the packet can be determined from Gaussian fits of the distribution. A series of such images for different holding times shows the time evolution of the angular position of
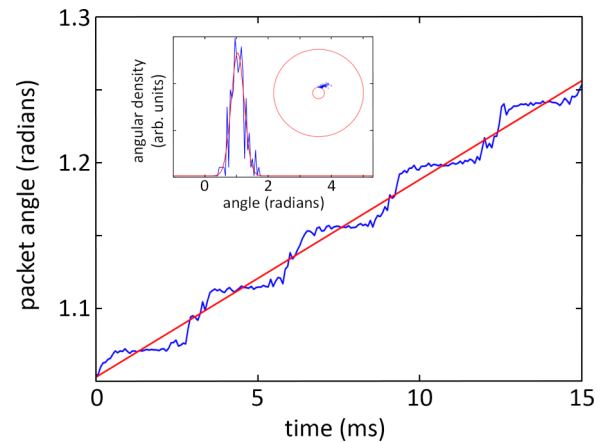

FIG. 8. (Color online) Angular momentum measurement method with *in situ* imaging. The main plot shows the average angular position of an atomic packet versus time (wiggly curve, blue online), along with a linear fit (straight line, red online) that gives the average angular velocity. The simulation is for an atomic packet that has returned to point A (i.e., A′) after completing the monodromy circuit of Fig. 2. Inset: Angular density of the packet (wiggly curve, blue online) and Gaussian fit (smooth curve, red online) versus angular position. The fit is used to determine the packet's average angle; the inset also shows a simulated image of the atoms (dots, blue online) in the ring potential along with the maxima and minima of the radial oscillations (circles, red online).

the packet. The main plot in Fig. 8 shows the results of a numerical simulation of this process: The average angular velocity $\langle \dot\theta \rangle$ is the overall slope of the angular time evolution, but the plot also contains a periodic step feature that reflects the radial oscillations of the atoms. The angular momentum L can be extracted from the time evolution of a packet's angular position, such as shown in Fig. 8, by determining the angle change $\Delta\theta_T$ over the course of one radial oscillation period ΔT_{radial} and then solving the following integral equation numerically for L [66]:

$$\Delta\theta_T = 2 \int_{R_{\min}}^{R_{\max}} \frac{L\,dr}{r^2 \sqrt{\frac{2}{m}[h - V(r)] - \frac{L^2}{m^2 r^2}}}, \qquad (14)$$

where h refers to the total energy of the atoms, $V(r)$ is the ring potential, and $R_{\min}$ and $R_{\max}$ are the inner and outer turning radii, respectively.

Extracting L requires knowledge of all the other quantities in Eq. (14). While $\Delta\theta_T$ can be determined from the step size of the "staircase" plot of average angular position versus time, it is more reliably obtained in our simulations from the relation $\Delta\theta_T = \Delta T_{\text{radial}}\langle \dot\theta \rangle$: The average angular velocity $\langle \dot\theta \rangle$ is the slope of a linear fit to the average angular position plot in Fig. 8, and the radial period ΔT_{radial} of the atomic packet in the ring potential can be obtained from a Fourier transform of the average angular position time series in Fig. 8. $V(r)$ can be determined experimentally by *in situ* absorption imaging of a cold thermal gas of temperature T_{thermal} in the ring potential: The image provides the radial atomic density $n(r)$ which can then be used to extract the potential through the relation $n(r) \cong \exp[-V(r)/kT_{\text{thermal}}]/\Lambda^3$, where $\Lambda = \hbar/\sqrt{2\pi m k T_{\text{thermal}}}$ is the thermal de Broglie wavelength [67]. The determination of the average total energy E of an atom in a packet was described in the previous section. The inner and outer turning radii can be determined from knowledge of the potential and the total energy or from *in situ* imaging. We find through numerical simulations of the above measurement method that L can be determined with an accuracy of 5%–10% over the course of the entire spectrum space path.

V. CONCLUSION

We have shown that a dynamical monodromy circuit can be implemented by ordinary forces, and we have described two ways to realize a dynamical monodromy circuit in a physical system—a puck on an air table, and an ultracold gas. All our calculations are classical, and presume no interaction between the particles, so measurements on a cold gas would raise questions about quantum behavior and about interactions between particles that are not addressed in this paper.

ACKNOWLEDGMENTS

APPENDIX A: NUMERICAL COMPUTATION OF CANONICAL ANGLE LOOPS

The method described here can be adapted for use in a great variety of systems, but we describe it here in detail for cylindrically symmetric systems. Given specified regular values of angular momentum $L(z) = l$ and energy $H(z) = h$ we presume that the corresponding torus is unique. For that specified (l,h), we choose a circle $\rho = \rho^0$ in the classically allowed region, and we choose an arbitrary point (ρ^0, ϕ^0) on that circle. At that point we set initial conditions on the momenta: $p_\phi^0 = l$ by definition, and p_ρ^0 is chosen as any value such that $H(p_\rho^0, p_\phi^0, \rho^0, \phi^0) = h$. Starting at that point, and time $t = t^0$ we integrate Hamilton's equations until the coordinate $\rho(t)$ passes again through the circle $\rho = \rho^0$ in the original sense (outward or inward, whichever way we started the trajectory), and we record the time of first return $\tau(l,h) = t - t^0$ and the subtended angle $\Delta(l,h) = \phi - \phi^0$, defined below. Now we define an effective Hamiltonian, which is a function of the four phase-space variables and two parameters (l,h),

$$\mathscr{H}(z;l,h) : \mathbb{R}^4 \times \mathbb{R}^2 \to \mathbb{R},$$
$$\mathscr{H}(z;l,h) \equiv \frac{[\tau(l,h)H(z) - \Delta(l,h)L(z)]}{2\pi}. \qquad (A1)$$

This is regarded as a function of the phase-space variables z, with l and h treated as fixed parameters. In other words, we derive equations of motion by differentiating $\mathscr{H}$ with respect to each z_i, holding l and h fixed. Here it is essential to distinguish between $[L(z), H(z)]$, the functions of positions and momenta, and their numerical values $[l,h]$, which are regarded as fixed parameters when Hamilton's equations are computed. In our case,

$$\mathscr{H}(z;l,h) \equiv \frac{1}{2\pi}\left\{ \tau(l,h)\left[\frac{p_\rho^2}{2} + \frac{p_\phi^2}{2\rho^2} + V(\rho) \right] - \Delta(l,h)p_\phi \right\} \qquad (A2)$$

and, for example, denoting σ as the timelike variable,

$$\frac{d\phi}{d\sigma} = \frac{\partial \mathscr{H}}{\partial p_\phi} = \frac{1}{2\pi}\left[\frac{\tau(l,h)p_\phi}{\rho^2} - \Delta(l,h) \right]. \qquad (A3)$$

Equations of motion for other variables are obtained similarly. (For $h > 0$ it is best to integrate in Cartesian coordinates to avoid singular behavior near the origin.) Numerical integration of this path $z(\sigma)$ from $\sigma = 0$ to 2π produces a γ_2 loop.

As we change l and h, going from one torus to another, we need to define a connection between angle variables on the changing tori such that the transformation between phase-space points and variables (ϕ_1, ϕ_2, l, h) is a differentiable and invertible transformation. To do this, we must give a definition of the origin of angle coordinates $\mathbf{z}^0(0,0,l,h)$ such that the angles are differentiable functions of $\mathbf{z}$, and a definition of $\Delta(l,h)$ such that it is a differentiable function of (l,h). In the present case, we may choose the outermost point of each torus on the x axis to be the origin of angle coordinates.

When we define Δ so that it changes smoothly, we find that it is forced to be a multivalued function of (l,h). In our case, starting with $(l = 0, h < 0)$, $\Delta(l,h) = 0$. Increasing l from
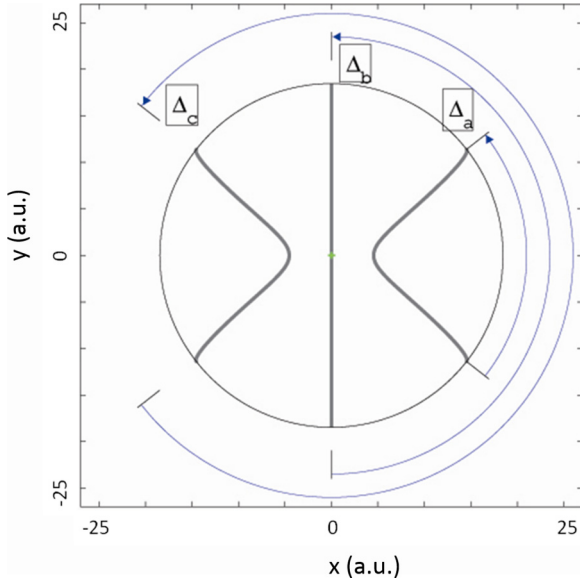
FIG. 9. (Color online) The angle $\Delta(l,h)$ must be defined such that it changes smoothly with l and h. As l decreases through zero with $h > 0$, $\Delta(l,h)$ must be defined so that it increases smoothly through π.

there makes $\Delta(l,h)$ small and positive. Proceeding around the monodromy circuit, $\Delta(l,h)$ increases until at $l = 0, h > 0$, $\Delta(l,h) = \pi$. As l goes negative with $h > 0$, $\Delta(l,h)$ must be defined so that it and all its derivatives with respect to l and h are continuous. This is done by defining $\Delta(l,h)$ as shown in Fig. 9. Δ is therefore a multivalued function of (l,h): The monodromy point $(l = 0, h = 0)$ is a branch point, and $\Delta(l,h)$ changes from 0 to 2π on its journey around the monodromy circuit.

The resulting γ_2 loop also evolves smoothly, and displays monodromy, as was shown in Fig. 1. This is the method we used to create that figure.

The corresponding multivalued action variable $\mathscr{I}_2(l,h)$ can be computed by integration around that γ_2 loop,

$$\mathscr{I}_2(l,h) = \frac{1}{2\pi} \oint_{\gamma_2} \boldsymbol{p}(s) \cdot \frac{d\boldsymbol{q}}{ds} ds. \tag{A4}$$

To show that this is all consistent with more familiar definitions, let us examine

$$\mathscr{I}_2'(l_1,h_1) = \frac{1}{2\pi} \oint p_\rho(\rho;l,h)d\rho,$$

$$\mathscr{I}_2'(l_2,h_2) = \frac{1}{2\pi} \oint p_\rho(\rho;l,h)d\rho - l, \tag{A5}$$

where (l_1,h_1) are any values of (l,h) on the first half of the monodromy circuit, (l_2,h_2) are any values on the second half, and

$$p_\rho(\rho;l,h) = \left\{ 2\left[h - \frac{l^2}{2\rho^2} - V(\rho) \right] \right\}^{1/2}. \tag{A6}$$

One easily shows that $\mathscr{I}_2'$ defined in Eq. (A5) is the same as $\mathscr{I}_2$ defined in Eq. (A4), and

$$\frac{\partial \mathscr{I}_2'}{\partial h} = \frac{\tau(l,h)}{2\pi},$$

$$\frac{\partial \mathscr{I}_2'}{\partial l} = \frac{-\Delta(l,h)}{2\pi}. \tag{A7}$$

Hence we can write this action variable as a function of phase-space coordinates z with the notation

$$I_2(z) = \mathscr{I}_2'(L(z),H(z)), \tag{A8}$$

and its derivatives with respect to z are

$$\nabla_z I_2(z) = \left(\frac{\partial \mathscr{I}_2'}{\partial l} \right) \nabla_z L(z) + \left(\frac{\partial \mathscr{I}_2'}{\partial h} \right) \nabla_z H(z)$$

$$= \frac{1}{2\pi} [\tau(l,h)\nabla_z H(z) - \Delta(l,h)\nabla_z L(z)]. \tag{A9}$$

The conjugate angle ϕ_2 is obtained by using I_2 as Hamiltonian, and σ and ϕ_2 range from 0 to 2π on the γ_2 loop.

APPENDIX B: DETAILS OF THE APPLIED FORCES

The formulas for applied forces given below were obtained as a result of numerical experiments. We did not use any systematic optimization method to obtain these results, but only a modest number of trials. For single-loop initial conditions, we begin with N particles, all having angular momenta equal to 0, and all having the same initial energy, uniformly distributed around a γ_2 loop on the initial torus $[l(t_0) = 0, h(t_0) = h_0]$. At each instant they have a center of mass located at $\vec{r}_0(t)$, where

$$\vec{r}_0(t) = \frac{\sum_i^N m_i \vec{r}_i(t)}{\sum_i^N m_i} = r_0(t)\cos\varphi(t)\vec{i} + r_0(t)\sin\varphi(t)\vec{j}. \tag{B1}$$

$\vec{r}_i(t)$ and m_i are the instantaneous location vector and mass of the ith particle, and $r_0(t)$ and $\varphi(t)$ are the instantaneous length and azimuthal angle of the instantaneous center-of-mass vector $\vec{r}_0(t)$. As mentioned in the main section of this paper, the monodromy circuit is divided into five steps, with $t_{i-1} \leqslant t \leqslant t_i$ on the ith step.

The driving torque that changes the angular momentum is applied as follows. The same force $\vec{F}(t)$ is applied to all particles, and this force is nearly perpendicular to the center-of-mass vector $\vec{r}_0(t)$. The direction of the force is such that the angular momentum of the center of mass increases in step 1 and in step 5, and such that it decreases in step 3. Thus, in steps 1 and 5, $\vec{F}(t)$ is $\pi/2$ "ahead of" $\vec{r}_0(t)$:

$$\vec{F}(t) \equiv F(t)\cos\left[\varphi(t) + \frac{\pi}{2}\right]\vec{i} + F(t)\sin\left[\varphi(t) + \frac{\pi}{2}\right]\vec{j}, \tag{B2}$$

$$F(t) \equiv \frac{\dot{\Lambda}(t)}{\sqrt{\overline{r^2}(t)}}, \qquad \overline{r^2}(t) \equiv \frac{\sum_i^N m_i \vec{r}_i^2(t)}{\sum_i^N m_i}. \tag{B3}$$

$\overline{r^2}(t)$ is the mean square distance from the origin to the instantaneous location of each particle, and $\dot{\Lambda}(t)$ is a chosen average rate of increase of angular momentum. It is made to increase and decrease smoothly, as below. In steps 2 and 4,

$\dot{\Lambda}(t) = 0$, while in steps 1 and 3,

$$\dot{\Lambda}(t) = c_i \dot{\Lambda}_0 \text{sech}\left[\left(\frac{t_i - t_{i-1}}{2}\right)\left(\frac{1}{t_{i-1} - t} + \frac{1}{t_i - t}\right)\right]. \quad \text{(B4)}$$

$\dot{\Lambda}_0$ is a constant value which we take to be 0.9, and $c_i = 1, -2,$ and 3, respectively, in steps 1, 3, and 5. The negative sign in step 3 makes the force rotate in the same sense as the center of mass, but $\pi/2$ "behind," so the angular momentum is reduced in this step. Equation (B4) makes the torque change as a C^∞ function of time.

We found that a slightly different method worked best for step 5. We took for $t > t_4$,

$$\vec{F}(t) \equiv F_5 \cos\left[\varphi(t_4) + \omega t + \frac{\pi}{2}\right]\vec{i} + F_5 \sin\left[\varphi(t_4) + \omega t + \frac{\pi}{2}\right]\vec{j}, \quad \text{(B5)}$$

where $\varphi(t_4)$ is the azimuthal angle of the center of mass at time t_4, and ω is a constant rotation rate chosen to be

$$\omega \equiv \frac{\Delta(l(t_4), h(t_4))}{\tau(l(t_4), h(t_4))}, \quad \text{(B6)}$$

where $(l(t_4), h(t_4))$ are the average value of angular momentum and energy when $t = t_4$, and $\Delta(l, h)$ and $\tau(l, h)$ are defined in Appendix A as subtended angle and time of first return as functions of angular momentum and energy. F_5 is a constant and set to be 0.15.

During steps 2 and 4, while there is no driving torque, the parameters of the well are changed by changing the height of the central barrier. In our calculations this is done by changing the power in the strongly focused laser so that the height of the central barrier $V(t)$ varies continuously between V_0 and V_1 as follows.

$$V(t) = V_0 \quad \text{if} \quad 0 \leqslant t \leqslant t_1$$
$$= V_0 + (V_1 - V_0)\left\{\tanh\left[\left(\frac{t_2 - t_1}{2}\right)\left(\frac{1}{t_1 - t} + \frac{1}{t_2 - t}\right)\right]\right.$$
$$\left. + \frac{1}{2}\right\} \quad \text{if} \quad t_1 < t \leqslant t_2$$
$$= V_1 \quad \text{if} \quad t_2 < t \leqslant t_3$$
$$= V_1 + (V_0 - V_1)\left\{\tanh\left[\left(\frac{t_4 - t_3}{2}\right)\left(\frac{1}{t_2 - t} + \frac{1}{t_4 - t}\right)\right]\right.$$
$$\left. + \frac{1}{2}\right\} \quad \text{if} \quad t_3 < t \leqslant t_4$$
$$= V_0 \quad \text{if} \quad t_4 < t \leqslant t_5. \quad \text{(B7)}$$

Integration is stopped when the average value of the angular momentum returns to zero, and that defines the time t_5.

APPENDIX C: CLASSICAL DYNAMICAL MONODROMY ON AN AIR TABLE

This scheme is considerably simpler than the proposed ultracold atom implementation, but it is purely classical, and so while it can illustrate dynamical monodromy, it cannot address the interesting questions associated with quantum systems. In this approach, a puck on an air cushion serves as a single test mass which can move with negligible surface friction over a
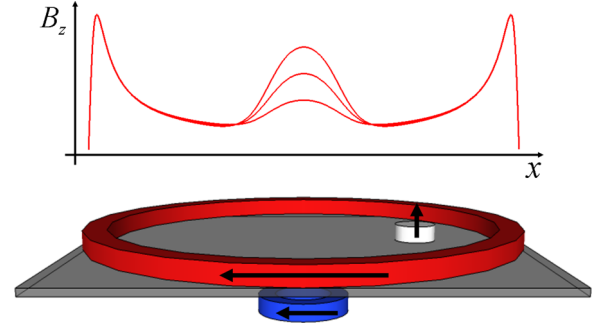

FIG. 10. (Color online) Magnetic confinement potential of the puck on the air table. Top: Plot of the magnetic field component normal to the air table, B_z, versus a radial horizontal axis. The horizontal confinement potential for the magnetic puck is proportional to B_z. The three curves plot B_z for central coil currents of $0.5I_0$, I_0, and $1.5I_0$, where I_0 is the current in the large outer coil. Both coils have the same number of turns. Bottom: Side view sketch of the air table (horizontal plane, gray online), large magnetic coil (red online), and central barrier magnetic coil (blue online). The arrows represent the direction of the current in the coils and the magnetic moment of the puck. The puck moves in a plane just above the surface of the air table.

horizontal planar surface. Magnetic forces are used to provide a ringlike confining potential in the horizontal plane, while the tilt of the air table away from horizontal provides an external force that exerts a torque on the puck. The motion of the puck can be recorded by a video camera placed directly above the air table. Repeating the circuit with different initial conditions and superposing the videos, one can watch the evolution of a loop.

Magnetic ring potential. A magnetic puck with a vertically oriented magnetization axis with magnetic moment $\vec{\mu}$ will experience a conservative potential in an external magnetic field, $\vec{B}$. The magnetic interaction Hamiltonian is $-\vec{\mu} \cdot \vec{B}$ and so it is proportional to the vertical component of $\vec{B}$. As shown in Fig. 10, a large diameter magnetic coil in the horizontal plane of motion of the puck provides the outer barrier of the ring potential, while a smaller concentric coil located below the air table provides the central barrier of the ring potential. The amplitude of the central barrier can be dynamically adjusted by varying the current flowing through it.

Torque force. The torque is provided by a uniform external force derived from Earth's gravity by tilting the air table by an angle ϑ from horizontal, in the desired direction of the force. The magnitude of the component of the force on the puck in the plane of the air table is then $mg\sin\vartheta$, where m is the mass of the puck. A directional and dynamically controlled tilt can be implemented by supporting the air table from below with a pivot point at its center and two electrically controlled actuator legs at adjacent corners. The height of the two legs can be modulated by independent computer controlled voltage signals. For a typical puck mass of 0.2 kg and a magnetic ring potential, such as in Fig. 10, with an outer radius on the order of 0.3 m produced by coils with currents on the scale of 200 amp-turns, our simulations show that the proper torque force can be produced with air table tilts on the order of 0.5° or less.

In this case, the equivalent spectrum space monodromy circuit can be completed on a time scale of 10–20 s.

Initial conditions. The puck is set in radial motion by holding it against the outer magnetic coil ring and then releasing it. The puck will travel radially, tracing out the ring of initial conditions in phase space, and the specific initial condition of interest is then selected by starting the monodromy process (i.e., the application of the torque force) when the puck has the required position and velocity.

Detection. The motion of the puck throughout the air table ring potential can be recorded by a video camera placed directly above the apparatus. The video provides the position of the puck as a function of time, from which the velocity of the puck can be derived. The position of the puck can be used to determine its magnetic potential energy (in combination with a magnetic field map), while the velocity gives its kinetic energy, and thus the total energy. The angular momentum can be derived from the velocity and radial position of the puck. The spectrum space path can thus be reconstructed from the energy and angular momentum of the puck.

Following a loop of initial conditions. The video would show each path $\mathbf{q}(t) = [x(t), y(t)]$, and superposition of the videos for different initial conditions would show the evolution of the whole loop.

APPENDIX D: MONODROMY AND HANNAY ANGLES

We are often asked about the relationship between monodromy and the phenomena associated with Hannay angles. There are some similarities, but there are also some essential differences.

Hannay [68] posed and answered the following question: Given an integrable Hamiltonian system; given that the trajectory begins on one torus; given that the Hamiltonian depends on one or more parameters; given that we change those parameters slowly so that they go around a cycle, returning to their initial values; then the adiabatic proposition asserts that the action variables will remain always constant, and therefore the system will return to its original torus. However, what happens to the angle variables?

Hannay showed that the angles evolve with time at the frequencies on the instantaneous tori, but with also a correction related to the integral of a certain 2-form. What

are the similarities and differences from our description of monodromy? Both situations involve changes of canonical angles. In both cases, one component of the change is the frequency on instantaneous tori. However there are several important differences.

Hannay's theory applies to systems with one or more degrees of freedom, while monodromy can only appear in systems with two or more degrees of freedom. (2) The Hannay angle describes the change of position of particles along a loop. When one goes around a circuit in the parameter space, the loop returns to its original form, but the particles are not in the same location. In contrast, in a system with monodromy, not only do particles change their positions around a loop, but the whole loop changes its structure. (3) The correction in Hannay's case is a geometrical integral over an area subtended by changing parameters, and it can have any value. However, monodromy is a topological phenomenon. The change of structure of the loop does not depend on an area. When the system goes around any circuit enclosing a monodromy point in a given sense we get a change which is independent of path. (4) Hannay's formulas apply only to adiabatic traversals of a circuit. Monodromy is quite different. (a) In our case, we drive the system so that the angular momentum changes—but angular momentum is an action variable, so an action is changing, so the system is not undergoing strictly adiabatic evolution. (b) Nevertheless, one might argue that we are imposing a kind of adiabatic evolution because we make the particles undergo several radial oscillations while moving from one torus to another—this helps keep the particles moving together from torus to torus. That is a correct description—our implementation is adiabatic in this sense. (c) However, we claim that *in principle*, monodromy does not require any adiabatic traversal of a circuit. The kind of ideal evolution described in [2] will give the same result whether the system goes rapidly or slowly. (d) On the other hand, in practice, the only way we know how to implement a monodromy circuit in a real classical system with real forces involves a separation of time scales. In our case, we want all the particles to have nearly equal angular momenta; however, when the same force is applied to all particles, the ones at small radius experience a smaller torque and therefore a smaller change of angular momentum. Thus, in principle, monodromy does not require adiabaticity, but in actual implementation, it probably does.

[1] J. B. Delos, C. R. Schleif, and G. Dhont, J. Phys.: Conf. Ser. **99**, 012005 (2008).

[2] J. Delos, G. Dhont, D. Sadovskií, and B. Zhilinskií, Ann. Phys. **324**, 1953 (2009).

[3] V. I. Arnold, *Geometrical Methods in the Theory of Ordinary Differential Equations* (Springer, New York, 1988).

[4] I. C. Percival, J. Phys. B **6**, L229 (1973).

[5] I. Percival, in *Stochastic Behavior in Classical and Quantum Hamiltonian Systems*, edited by G. Casati and J. Ford, Lecture Notes in Physics Vol. 93 (Springer, Berlin, 1979), p. 259.

[6] I. Percival, in *Nonlinear Dynamical Aspects of Particle Accelerators*, Lecture Notes in Physics Vol. 247 (Springer, Berlin, 1986), pp. 12–36.

[7] D. W. Noid and R. A. Marcus, J. Chem. Phys. **62**, 2119 (1975).

[8] D. W. Noid and R. A. Marcus, J. Chem. Phys. **67**, 559 (1977).

[9] D. W. Noid and R. A. Marcus, J. Chem. Phys. **85**, 3305 (1986).

[10] D. W. Noid, M. L. Koszykowski, and R. A. Marcus, J. Chem. Phys. **71**, 2864 (1979).

[11] D. W. Noid, M. L. Koszykowski, and R. A. Marcus, J. Chem. Phys. **73**, 391 (1980).

[12] D. W. Noid, M. L. Koszykowski, and R. A. Marcus, Annu. Rev. Phys. Chem. **32**, 267 (1981).

[13] S. K. Knudson, J. B. Delos, and D. W. Noid, J. Chem. Phys. **84**, 6886 (1986).

[14] S. K. Knudson and D. W. Noid, Chem. Phys. Lett. **145**, 16 (1988).

[15] D. W. Noid, M. L. Koszykowski, and R. A. Marcus, in *Quantum Mechanics in Mathematics, Chemistry and Physics*, edited by K. E. Gustafson and W. P. Reinhardt (Plenum, New York, 1981), p. 133.

[16] B. G. Sumpter and D. W. Noid, Chem. Phys. Lett. **126**, 181 (1986).

[17] M. V. Berry, in *The Wave-Particle Dualism: A Tribute to Louis de Broglie on his 90th Birthday*, edited by S. Diner (Springer, Berlin, 1984), pp. 231–252.

[18] A. M. O. De Almeida, *Hamiltonian Systems: Chaos and Quantization* (Cambridge University Press, Cambridge, UK, 1990).

[19] R. Swimm and J. Delos, J. Chem. Phys. **71**, 1706 (1979).

[20] R. T. Swimm and J. B. Delos, J. Chem. Phys. **78**, 4795 (1983).

[21] M. K. Ali and S. S. Kipp, J. Phys. A: Math. Gen. **27**, 1953 (1994).

[22] K. M. Atkins and G. S. Ezra, Phys. Rev. E **51**, 1822 (1995).

[23] D. M. Wardlaw, D. W. Noid, and R. A. Marcus, J. Phys. Chem. **88**, 536 (1984).

[24] J. Gao and J. B. Delos, Phys. Rev. A **49**, 869 (1994).

[25] V. Kondratovich and J. B. Delos, Phys. Rev. A **57**, 4654 (1998).

[26] K. Richter and D. Wintgen, J. Phys. B **24**, L565 (1991).

[27] K. Richter, G. Tanner, and D. Wintgen, in *Quantum Chaos: Between Order and Disorder*, edited by G. Casati and B. Chirikov (Cambridge Uniuversity Press, Cambridge, 1995), p. 287.

[28] D. Wintgen and K. Richter, Comments At. Mol. Phys. **29**, 261 (1994).

[29] R. G. Littlejohn and W. G. Flynn, Phys. Rev. A **45**, 7697 (1992).

[30] M. T. Lopez-Arias, V. R. Manfredi, and L. Salasnich, La Rivista del Nuovo Cimento, Ser. 3 **17**, 1 (1994).

[31] B. H. Lavenda, Open Syst. & Information Dyn. **10**, 51 (2003).

[32] R. H. Cushman and L. M. Bates, *Global Aspects of Classical Integrable Systems* (Birkhäuser, Basel, 1997).

[33] J. J. Duistermaat, Commun. Pure Appl. Math. **33**, 687 (1980).

[34] L. M. Bates, Z. Angew. Math. Phys. **42**, 837 (1991).

[35] M. Zou, J. Geom. Phys. **10**, 37 (1992).

[36] R. Cushman and J. J. Duistermaat, Bull. Am. Math Soc. **19**, 475 (1988).

[37] R. Cushman and D. Sadovskii, Physica D **142**, 166 (2000).

[38] K. Efstathiou, D. A. Sadovskii, and B. I. Zhilinskii, Proc. R. Soc. London, Ser. A **463**, 1771 (2007).

[39] K. Efstathiou, O. V. Lukina, and D. A. Sadovskii, Phys. Rev. Lett. **101**, 253003 (2008).

[40] R. Cushman, H. Dullin, A. Giacobbe, D. Holm, M. Joyeux, P. Lynch, D. Sadovskii, and B. Zhilinskii, Phys. Rev. Lett. **93**, 024302 (2004).

[41] M. Sanrey, M. Joyeux, and D. A. Sadovskii, J. Chem. Phys. **124**, 074318 (2006).

[42] A. Giacobbe, R. Cushman, D. Sadovskii, and B. Zhilinskii, J. Math. Phys. **45**, 5076 (2004).

[43] K. Efstathiou, M. Joyeux, and D. Sadovskii, Phys. Rev. A **69**, 032504 (2004).

[44] M. Joyeux, D. Sadovskii, and J. Tennyson, Chem. Phys. Lett. **382**, 439 (2003).

[45] L. Grondin, D. A. Sadovskii, and B. I. Zhilinskii, Phys. Rev. A **65**, 012105 (2001).

[46] D. Sadovskii and B. Zhilinskii, Phys. Lett. A **256**, 235 (1999).

[47] K. Efstathiou, R. Cushman, and D. Sadovskii, Adv. Math. **209**, 241 (2007).

[48] N. N. Nekhoroshev, D. A. Sadovskií, and B. I. Zhilinskii, Compt. Rendus Math. **335**, 985 (2002).

[49] N. N. Nekhoroshev, D. A. Sadovskií, and B. I. Zhilinskií, Ann. Henri Poincaré **7**, 1099 (2006).

[50] B. P. Winnewisser and M. Winnewisser, in *Fourier Transform Spectroscopy*, edited by A. Sawchuk, OSA Trends in Optics and Photonics Vol. 84 (Optical Society of America, Washington, DC, 2003).

[51] B. P. Winnewisser, M. Winnewisser, I. R. Medvedev, M. Behnke, F. C. De Lucia, S. C. Ross, and J. Koput, Phys. Rev. Lett. **95**, 243002 (2005).

[52] M. Winnewisser, B. P. Winnewisser, I. R. Medvedev, F. C. De Lucia, S. C. Ross, and L. M. Bates, J. Mol. Struct. **798**, 1 (2006).

[53] C. A. Arango, W. W. Kennerly, and G. S. Ezra, Chem. Phys. Lett. **392**, 486 (2004).

[54] C. R. Schleif and J. B. Delos, Phys. Rev. A **76**, 013404 (2007).

[55] C. R. Schleif and J. B. Delos, Phys. Rev. A **77**, 043422 (2008).

[56] N. J. Fitch, C. A. Weidner, L. P. Parazzoli, H. R. Dullin, and H. J. Lewandowski, Phys. Rev. Lett. **103**, 034301 (2009).

[57] S. Kulin, S. Aubin, S. Christe, B. Peker, S. L. Rolston, and L. A. Orozco, J. Opt. B: Quantum Semiclassical Opt. **3**, 353 (2001).

[58] R. Ozeri, L. L. Khaykovich, N. Friedman, and N. Davidson, J. Opt. Soc. Am. B **17**, 1113 (2000).

[59] G. D. Bruce, J. Mayoh, G. Smirne, L. Torralbo-Campo, and D. Cassettari, Phys. Scr. T **143**, 014008 (2011).

[60] N. Friedman, L. Khaykovich, R. Ozeri, and N. Davidson, Phys. Rev. A **61**, 031403 (2000).

[61] G. Roati, M. Zaccanti, C. D'Errico, J. Catani, M. Modugno, A. Simoni, M. Inguscio, and G. Modugno, Phys. Rev. Lett. **99**, 010403 (2007).

[62] W. Ketterle, D. S. Durfee, and D. M. Stamper-Kurn, in *Proceedings of the Enrico Fermi International School of Physics, Course CXL*, edited by M. Inguscio, S. Stringari, and C. E. Wieman (IOS Press, Amsterdam, 1999), p. 67.

[63] S. Chiow, T. Kovachy, H. C. Chien, and M. A. Kasevich, Phys. Rev. Lett. **107**, 130403 (2011).

[64] D. M. Giltner, R. W. McGowan, and S. A. Lee, Phys. Rev. A **52**, 3966 (1995).

[65] W. Petrich, M. H. Anderson, J. R. Ensher, and E. A. Cornell, Phys. Rev. Lett. **74**, 3352 (1995).

[66] L. D. Landau and E. M. Lifshitz, *Mechanics: Course of Theoretical Physics* (Butterworth-Heinemann, Oxford, 1976), Vol. 1

[67] V. Bagnato, D. E. Pritchard, and D. Kleppner, Phys. Rev. A **35**, 4354 (1987).

[68] J. Hannay, J. Phys. A: Math. Gen. **18**, 221 (1985).